Composites: Part A 200 (2026) 109361

Contents lists available at ScienceDirect

Composites Part A

journal homepage: www.elsevier.com/locate/compositesa

Correlating fibre break development with fibre misalignment and resin-rich pockets using *in situ* holotomography

Yeajin Lee [a,*], Thanasis Chatziathanasiou [b], Christian Breite [b], Mahoor Mehdikhani [b], Yentl Swolfs [b], Mark N. Mavrogordato [a], S. Mark Spearing [a], Ian Sinclair [a]

[a] μ-VIS X-ray Imaging Centre, University of Southampton, United Kingdom
[b] Department of Materials Engineering, KU Leuven, Belgium

HIGHLIGHTS

- *In situ* 150 nm synchrotron holotomography monitors fibre breaks under tension.
- Misplaced/misaligned fibres and resin-rich pockets influence break development.
- Interactions promote break clustering and microscale damage near breaks.
- Clusters reveal severe matrix nonlinearity via matrix microcracks and debonds.
- Local microstructural variations act as precursors to fibre break development.

GRAPHICAL ABSTRACT

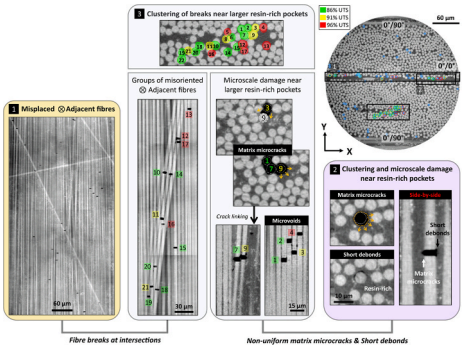

ARTICLE INFO

Keywords:
A. Polymer-matrix composites (PMCs)
B. Microstructural variations
C. Fibre breaks
D. Synchrotron holotomography

ABSTRACT

Understanding the mechanical influence of microstructural variations on fibre break development is crucial for reducing uncertainties in predicting the longitudinal tensile failure of unidirectional composites. In this study, the interaction between local microstructural variations and fibre breaks is monitored using *in situ* X-ray holotomography at 150 nm voxel size. Three distinctive microstructures are identified to drive the initiation and clustering of breaks. First, misplaced fibres within the 0°/0° interply region, exhibiting significant misorientation and intersecting multiple aligned fibres, progressively trigger multiple single breaks and a co-planar cluster at their intersections. Second, resin-rich pockets within the 0°/0° interply region influence break clustering, progressively forming a non-coplanar cluster of five breaks, accompanied by non-uniform matrix microcracks and short interfacial debonds surrounding the clusters. Third, large resin-rich pockets, locally formed in regions with misoriented fibre groups, play a critical role in driving pronounced break clustering. Their interactions exhibit severe matrix nonlinearity, as evidenced by matrix microcracks, short interfacial debonds, and damage features, including microvoids or the onset of matrix microcracks. The identified fibre break patterns, clustering behaviour, and damage associated with three microstructural cases provide new insights into how these microstructures serve as precursors to fibre break development, highlighting the importance of accounting for them in predicting longitudinal tensile failure to improve reliability.

* Corresponding author.
E-mail address: yeajin.lee@soton.ac.uk (Y. Lee).

https://doi.org/10.1016/j.compositesa.2025.109361
Received 23 May 2025; Received in revised form 11 September 2025; Accepted 14 October 2025
Available online 15 October 2025

1. Introduction

Fibre-reinforced composites are now widely used in structural applications across many sectors, such as automotive, aerospace, construction, and renewable energy. Despite their widespread use, the relatively brittle structural response of carbon fibre-epoxy composites remains a key challenge in material development and structural design. In tensile-dominated failure, the fibre-direction material response is also essentially elastic-brittle. It is widely recognised that, in most cases, the ultimate tensile final failure of multidirectional composites is determined by the failure of fibres oriented in the principal loading direction [1]. Therefore, a fundamental understanding of longitudinal failure in 0° plies of unidirectional (UD) composites is crucial for the reliable prediction of the final failure.

The failure process of 0° plies is reported to involve various damage mechanisms, including fibre breaks, fibre–matrix interfacial debonding, and matrix cracking. The widely accepted failure scheme begins with the weakest fibres failing, in accordance with some form of Weibull strength distribution [2,3]. After fibre breaks, stress is transferred from the broken fibre to the matrix, and then to neighbouring fibres via shear-dominated deformation of both the matrix and the interface. While the broken fibre experiences increasing tensile stress gradients on either side of the break, neighbouring fibres immediately adjacent to the break are subjected to stress concentrations, increasing their failure probability. As a result, additional breaks emerge in the vicinity of pre-existing ones, creating break clusters [1,4–11]. As the load increases, some break clusters progressively grow in size while new ones emerge nearby, eventually forming a critical self-sustaining cascade [12–14].

Many studies have investigated stress redistribution around single and clustered fibre breaks using shear-lag analysis [5–8,15] and finite element (FE) models [12,16–20], adopting a variety of simplifications to predict stress redistribution. These typically assume idealised conditions with 2D/3D regular fibre packings [4,6,19,21], elastic or viscoelastic matrix behaviour, and perfectly bonded interfaces. More complex simulations have incorporated random fibre packings, elastoplastic matrix behaviour, and the presence of interfacial debonds [18,20,22,23]. However, uncertainties persist in these predictions, particularly because most models do not account for manufacturing-induced microstructural variations, such as severe local fibre misalignment and resin-rich pockets. In recent years, X-ray micro-computed tomography (μCT), particularly Synchrotron Radiation Computed Tomography (SRCT), has enabled 3D, *in situ*, imaging of composites at spatial resolutions sufficient to distinguish individual fibre breaks [24–26] and to correlate with microstructural features [27–29]. This has catalysed the opportunity for a deeper understanding of how variations in microstructural features influence fibre breaks and, more broadly, composite strength in both experimental and numerical studies.

Rosini *et al.* [29] examined the differences in local fibre misorientation and nearest neighbour distances between break and intact sites. Their statistical results demonstrated that fibres at single break sites have a higher standard deviation in their orientation distribution compared to intact fibre sites. Clustered breaks, such as planar duplets, were also shown to occur preferentially in regions with a locally high fibre volume fraction. Breite *et al.* [12] observed similar break behaviour through *in situ* SRCT, linking clustered breaks to fibre regions with significant in-plane misalignment. Findings from both studies remain limited to the initiation of clustered breaks, without elucidating the damage mechanisms that drive their formation and subsequent progression, or how clusters interact with local microstructural variations under increasing loads. In this context, Fritz *et al.* [30] used μCT to identify microstructural features in aerospace-grade UD carbon fibre composites, including tow-aligned resin-rich pockets at ply interfaces and sub-microvoids distributed throughout the laminate. The study also reported on the presence of *misplaced* fibres at ply interfaces, which deviate markedly from the main UD ply orientation and intersect multiple neighbouring fibres (as opposed to *misaligned* fibres, which may deviate from the nominal ply direction but are entirely constrained to their local tow).

FE models incorporating microstructural variations have also addressed their effects on stress localisation and composite strength. Malgioglio *et al.* [31] developed FE models of a UD carbon/epoxy ply, incorporating variability in fibre misalignment and fibre volume fraction, and examined their effect on longitudinal tensile strength. Increasing material variability led to reduced strength and greater scatter in predicted values, with fibre misalignment playing a dominant role. This study, however, leaves a gap in predicting how material variability contributes to composite failure, primarily due to two key aspects. First, the FE models are limited to the ply level, thereby not addressing how material variability interacts with composite constituents at the fibre level, nor how this interaction contributes to strength reduction. Second, local fibre misalignment replicated with misorientation angles of −2° to 2° remains insufficient to fully capture the range observed in commercially manufactured composites. Recently, Jafarypouria *et al.* [22] implemented microscale FE models of UD glass fibre bundles to examine stress redistribution around a single fibre break in both misaligned and perfectly aligned fibres, by measuring stress concentration factors (SCFs). The misaligned fibre models, based on misorientation ranging from 1.4° to 5°, again limit the ability to capture the local misalignment effects observed in some commercial products. Misaligned fibres were found to increase the maximum SCFs by ~ 33 % in neighbouring intact fibres at a fibre volume fraction of 50 %, which would suggest a significant increase in local failure probability.

Although the studies discussed above have advanced the understanding of how local microstructural variations relate to tensile failure, two important questions remain open for further investigation:

- If fibres exhibit local misalignment exceeding the small angles typically studied (<5°), similar to the misplaced fibres reported by Fritz *et al.* [30], how do severely misaligned fibres interact with aligned fibres, and how does this influence break behaviour under tensile loading?
- When fibres break at sites with local microstructural variations, how do the localised stresses interact with the surrounding matrix and fibre–matrix interfaces, and how might the resulting damage cause clustering of fibre breaks?

Whilst SRCT has been shown to be a valuable tool for understanding composite failure, imaging at voxel sizes finer than ~ 500 nm is rarely conducted, reflecting trade-offs between spatial resolution, field of view, and constraints in image acquisition. Given the scale of carbon fibres and typical fibre separation distances, isolated matrix microcracks and interfacial debonds may not be reliably detected, because openings may be smaller than 30 % of the voxel size [32]. Secondly, even if such processes are present, they can be obscured due to bright fringes surrounding discontinuities such as fibre breaks, commonly observed in SRCT based on propagation-based imaging (also known as in-line phase contrast) [33–35]. These fringes typically originate from break edges, hindering clear identification of damage features. To address these imaging limitations, Chatziathanasiou *et al.* [36,37] conducted the first *in situ* X-ray holotomography of composites at a 150 nm voxel size. This technique, based on propagation-based phase contrast nano-imaging, combined with the high resolution, enabled the detection of interfacial debonds and matrix cracks initiated from fibre breaks in glass and carbon fibre composites.

In this work, we extend the use of 150 nm *in situ* holotomography to elucidate interactions between local microstructural variations and fibre breaks under longitudinal tensile loading. The features studied span from the initiation of breaks to their progression into clusters, along with associated damage mechanisms, such as matrix microcracks and interfacial debonds. In particular, we focus on three distinctive microstructures influencing fibre break development: (i) misplaced fibres, i.e. fibres crossing several other fibres, (ii) resin-rich pockets, and (iii) larger

resin-rich pockets locally formed along groups of misoriented fibres. Fibre break behaviour and damage patterns linked to these microstructures have not been previously reported. Furthermore, the analysis was complemented by independent 650 nm scans from a different batch of the same material, confirming that the identified break interactions reflect a broader phenomenon beyond the studied samples. This study is the first to link local microstructural variations to fibre break behaviour at 150 nm voxel size, elucidating how they promote fibre break development.

2. Materials and methods

2.1. Materials

Two laminates of the same carbon fibre/epoxy prepreg were provided by Mitsubishi Chemical Corporation: (1) a $[90/0]_s$ cross-ply layup with a total thickness of ≈ 0.5 mm, and (2) a $[90_2/0_2]_s$ cross-ply layup with a total thickness of ≈ 1 mm. The $[90/0]_s$ and $[90_2/0_2]_s$ laminates were used for scanning at 150 nm and 650 nm voxel sizes, respectively. This matched the total thickness of the 0° plies to the available field of view (FOV) for the relevant imaging setups. MRZ65-18000 carbon fibre (Mitsubishi Chemical Corporation) was used, with a nominal fibre diameter of 5.4 μm and a tensile modulus of 287 GPa. The matrix resin was #350 series, amine-cured toughened epoxy (Mitsubishi Chemical Corporation). The prepreg laminates were cured in an autoclave according to standard aerospace-grade processing conditions, except that the curing temperature was 130 °C. The epoxy matrix was doped with silicon dioxide particles (SiO_2, 500 nm, near-spherical) to create random volumetric speckle patterns that facilitate digital volume correlation (DVC). The concentration of SiO_2 particles was limited to ~ 10 wt% of the resin, equivalent to 2.3 vol%. This combination of particle properties was selected to minimise impact on the mechanical behaviour of the polymer matrix system, as suggested in [36,38–40]. Whilst DVC analysis was carried out for these materials/tests, the results will be presented in a related subsequent publication currently in preparation by the authors.

2.2. Specimen design

Two configurations of the double-notched tensile specimens, with section widths of 0.8 mm and 1 mm between the notch roots, were prepared for *in situ* tensile testing via 150 nm and 650 nm scans, respectively (see section 2.3). Sample geometries are described in further detail in [25,36], with notches being introduced to localise damage to the volume scanned by SRCT. The volume fraction of 0° fibres in the notch region was measured from the 3D reconstructed volume, with 48.5 % for the 150 nm and 50 % for the 650 nm scan. The specimens were machined using waterjet cutting, a method used previously for machining similar specimens without causing significant damage [41]. Straight and T-shaped aluminium tabs, 1.5 mm thick, were attached to both faces and both ends of specimens used for 150 nm and 650 nm scans using aerospace adhesive, Scotch-Weld™ EC-9323B/A (3 M Company, Maplewood, MN, USA), to aid loading and mitigate stress concentrations at the specimen ends [42].

Prior to the *in situ* experiments at ID16B and ID19, e*x situ* tensile tests were performed on n (number) of specimens to determine the ultimate tensile strength (UTS) specific to the notch region. The measured UTS values were 2545 ± 168 MPa (n = 5, two 0° plies, 150 nm scan configuration) and 3008 ± 67 MPa (n = 5, four 0° plies, 650 nm scan configuration). Previous testing of similar cross-ply samples has shown that extensive delamination of the 90° plies and splitting of the 0° plies occur well before final failure, thereby isolating the 0° plies between the notch tips. Accordingly, this is deemed not to influence the failure development in the 0° plies [24]. Since the 0° plies were expected to primarily determine the longitudinal tensile failure of both specimens, only their cross-sectional area prior to 0° fibre splitting was considered in calculating the UTS. These average UTS values served as reference values for determining the stepwise loads applied during *in situ* testing.

To meet the specific requirements of the two beamlines used in this work and the related sample mounting stages, different loading rigs were used. For the 150 nm scans at ID16B, the tests were performed using a manual loading rig (via a bolt thread) equipped with a 1 kN load cell, manufactured in-house at KU Leuven, with scans being taken at five different levels (5 %, 67 %, 86 %, 91 %, 96 %) of the measured UTS. For the 650 nm scans at ID19, a modified Deben CT5000 single-actuator electromechanical rig was used, operating at a displacement rate of 0.2 mm/min, with scans being taken at four different levels (7 %, 89 %, 94 %, 99 %) of the measured UTS. A detailed description of each rig is provided in [29,36].

2.3. Synchrotron Radiation computed tomography

2.3.1. Imaging parameters for the 150 nm scan

In situ SRCT experiments were undertaken at 150 nm voxel size on the ID16B beamline of the European Synchrotron Radiation Facility (ESRF), Grenoble, France [43]. A 2048 × 2048 pixel^2 detector (PCO Edge 4.2 CLHS sCMOS) was used, with geometrical magnification resulting in effective pixel size of 150 nm. To increase the volume over which damage may be detected, two consecutive scans were taken along the gauge length at each load, with 250 pixels overlap in the FOV between them. This results in a total FOV of 3846 × 2048 pixel^2, equivalent to ≈ 0.6 × 0.3 mm^2. A "pink" beam with an energy of 29.6 keV was used ($\Delta E/E \simeq 10^{-2}$) [43]. Each scan acquired 2505 projections at four different sample-to-detector distances, producing four distinct holograms, with an exposure time of 10 ms per projection. Data reconstruction was undertaken using in-house software at the ESRF, with Paganin's phase retrieval algorithm applied to enhance phase contrast [44]. A detailed description of the reconstruction procedure can be found in [45–47]. Table 1 summarises the imaging parameters described above, together with those for the 650 nm scan presented in the following section.

2.3.2. Imaging parameters for the 650 nm scan

In situ SRCT experiments were conducted at 650 nm voxel size on the ID19 beamline of the ESRF. A 2560 × 2160 pixel^2 detector (PCO Edge 5.5 CLHS sCMOS) was coupled with a 10x magnification optic to achieve an effective pixel size of 650 nm, resulting in a FOV of ≈ 1.66 × 1.40 mm^2. A pink beam with a peak energy of 29 keV was used, and 1800 projections were acquired per scan with an exposure time of 100 ms per projection. CT image acquisition was performed over 180°, with a sample-to-detector distance of ≈ 50 mm, yielding a degree of phase edge enhancement in the resultant data. Tomographic reconstruction was performed using in-house developed reconstruction software (Nabu/Tomwer) at ESRF [48], with Paganin's phase retrieval applied prior to filtered back projection.

Table 1
Summary of synchrotron imaging acquisition parameters for the 150 nm and 650 nm scans.

Scan ID	150 nm Scan	650 nm Scan
Synchrotron beamline	ESRF ID16B	ESRF ID19
Imaging technique	X-ray nano-holotomography with phase contrast	Propagation-based phase-contrast X-ray imaging
Pixel size [nm]	150	650
Field of view [pixel^2]	3846 × 2048	2560 × 2160
Beam energy [keV]	29.6	29
Exposure time per projection [ms]	10	100
Number of projections	2505	1800

2.4. Image processing

Analysis of the fibre breaks and the associated microstructural variations was performed using Fiji™ ImageJ and Avizo 2023 software. As the initial image processing step, the reconstructed volumes in 16-bit (150 nm scans) and 32-bit (650 nm scans) format were converted to 8-bit using ImageJ software.

Fig. 1a presents a representative XY slice of the 150 nm scan, showing cross-sections of 0° and 90° fibre plies. The cross-sections of the 0° plies were labelled with black rectangles to mark regions where fibre breaks occurred in relation to misplaced fibres and resin-rich pockets in the 0°/0° interply and 0° intraply regions. Three key features (a-c) were identified in the labelled regions, with their corresponding image processing approaches described below.

a. Initiation and clustering of fibre breaks

Fig. 1a illustrates a stack along the Y-axis, hereafter referred to as the Y-axis stack, cropped from the 150 nm scan with reference to the region labelled as 'Region 1′. Fibre breaks are depicted in two orthogonal views (i.e., XY and XZ planes), with the breaks seen as distinct dark features. To track fibre break initiation and cluster development, breaks were identified at each scan load level, with their precise locations confirmed by inspection in at least two orthogonal views.

The magnified view of Region 1 illustrates the 2D visualisation of fibre breaks accumulated up to the final scan load. Given the alignment characteristics of UD composites, 2D visualisation was considered a suitable approach for identifying break sites by overlaying them onto the CT images. The following visualisation approaches were employed, in accordance with those presented in [36]. First, the Y-axis stack corresponding to each load level was projected along the Z-axis (i.e., the direction parallel to the fibre axis) using the *minimum intensity Z-projection* function in ImageJ. This resulted in the exclusive detection of the break features, with their size determined by their maximum diameters. Subsequently, masks were created for the projected breaks at each load, and their greyscale values were binarised into 80, 160, 240, corresponding to the first, second, and third load levels, respectively. Each mask was assigned a distinct colour in Avizo software to distinguish between scan load levels. Finally, the colour-coded masks were combined into a single 2D slice and overlaid onto a CT slice showing the 0° fibre cross-section, using the *color wash* module with the *Label 256* color map. The same cropping procedure and 2D visualisation were likewise applied to other labelled regions in the 150 nm scan, 'Region 2′ and 'Region 3′.

b. Influence of misplaced and misaligned fibres

As shown in Fig. 1a, the Y-axis stack of Region 1 reveals strongly misplaced fibres, labelled as 'fibre 1′, 'fibre 2′, *etc*. To visualise how misplaced fibres relate to fibre break development, the stack at the final scan load was projected along the Y-axis using the *average intensity Z-projection* function in ImageJ. The same procedure was likewise applied to groups of misoriented fibres.

c. Matrix microdamage near fibre breaks: interfacial debonds and matrix microcracks

Fig. 3b depicts the Y-axis stack of Region 2, containing clustered breaks (1 to 4) adjacent to resin-rich pockets within the 0°/0° interply region. Four XY slices (XY-1 to XY-4), taken perpendicular to the breaks, were extracted from the stack to examine microscale damage around the breaks. These slices are shown in Fig. 4a, where the *average* and *maximum intensity Z-projection* were used in ImageJ to delineate the fibre edges (white dash lines) and the extent of surrounding matrix cracking (orange dashed lines), respectively. As such, matrix microcracks can be observed extending non-uniformly into the matrix, alongside short partial debonds surrounding the breaks.

3. Results – Detected damage and local microstructural variations

3.1. Fibre breaks linked to misplaced fibres within the 0°/0° interply

This is the first report of fibre break behaviour occurring in regions

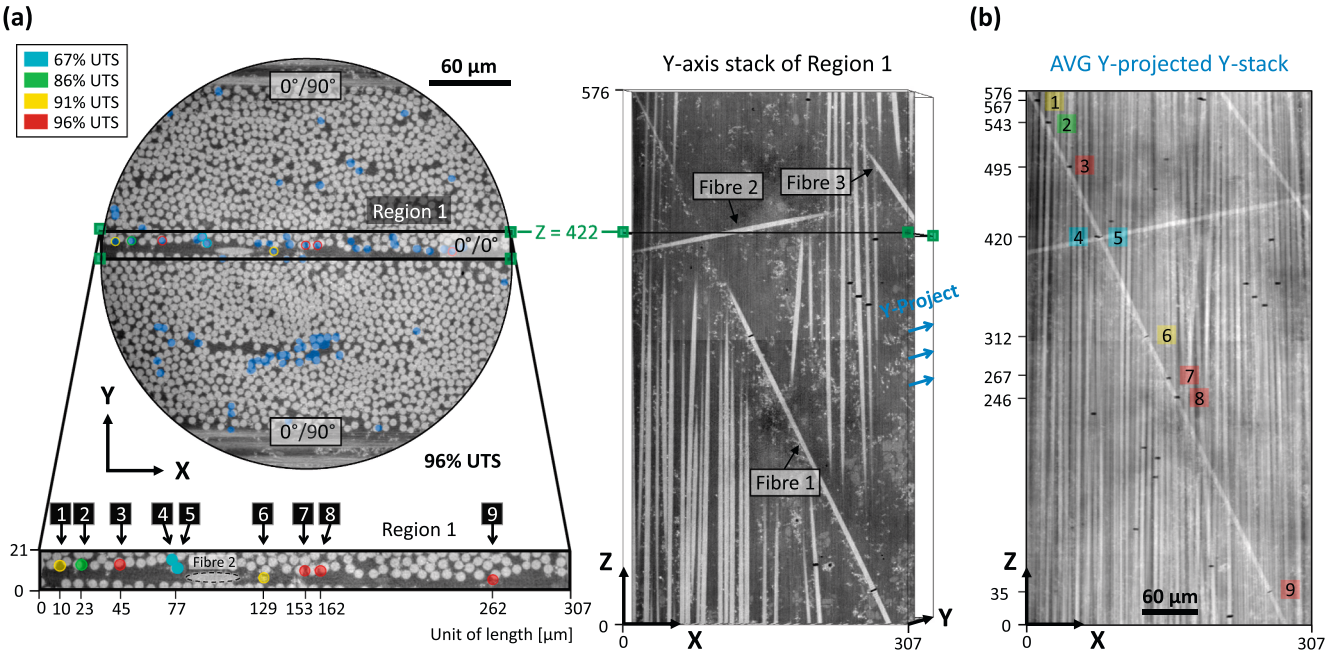

Fig. 1. 150 nm scan; SRCT images showing the fibre breaks interacting with misplaced fibres within the 0°/0° interply region. (a) An XY slice at Z = 422 µm, acquired at 96 % UTS within the scan volume containing two 0° plies, showing all breaks within this volume projected as blue dots. The black rectangle at the 0°/0° interply, labelled as 'Region 1′, marks the cropping region for the Y-axis stack. The magnified XY view of 'Region 1′ shows the projection of nine breaks linked to three misplaced fibres (1, 2, and 3), with dots colour-coded in cyan, green, yellow, and red, corresponding to their formation at 67 %, 86 %, 91 %, and 96 % UTS, respectively. (b) An XZ slice obtained from the average projection of the Y-axis stack along the Y-axis, revealing nine break sites at intersections between misplaced and adjacent fibres.

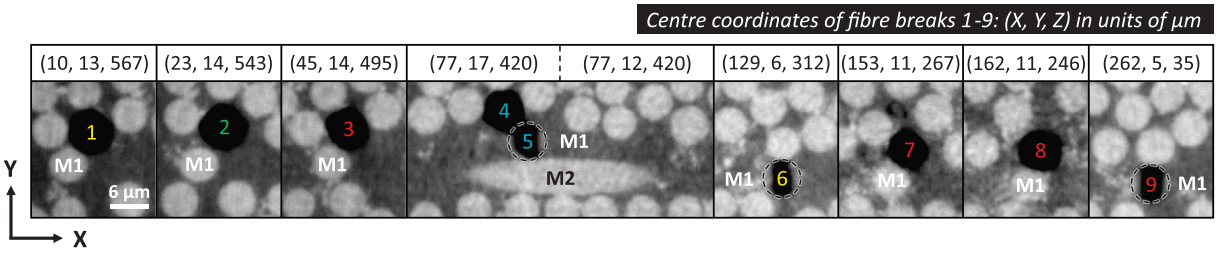

Fig. 2. 150 nm scan; Cross-sectional XY views of nine breaks formed within Y-stack of Region 1 (Fig. 1), which contains three misplaced fibres, showing their occurrence either within misplaced or adjacent fibres at intersections. Misplaced fibres 1 and 2 are labelled as M1 and M2, respectively. Each break number is colour-coded by formation load level, with centre coordinates defined relative to the XYZ axes of the Y-stack.

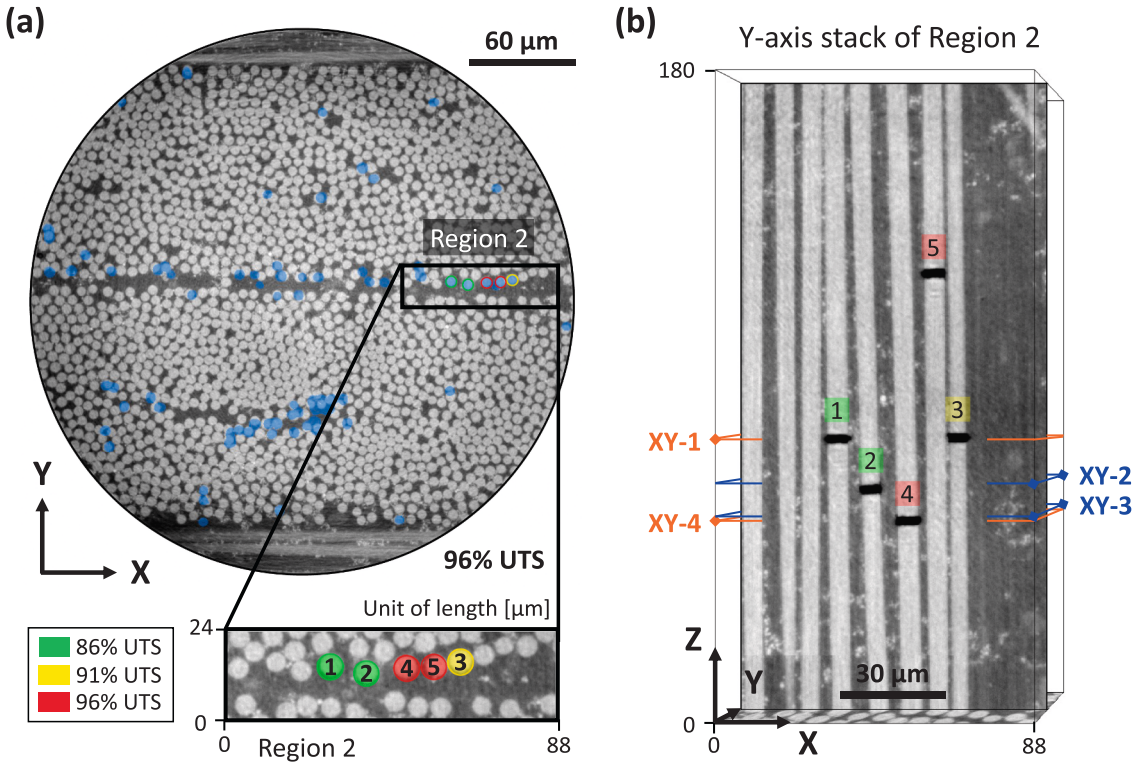

Fig. 3. 150 nm scan; SRCT images showing the fibre breaks interacting with resin-rich pockets within the 0°/0° interply region. (a) An XY slice acquired at 96 % UTS within the scan volume containing two 0° plies, showing all breaks within this volume projected as blue dots. The black rectangle at the 0°/0° interply, labelled as 'Region 2', marks the cropping region for the Y-axis stack. The magnified XY view of 'Region 2' shows the projection of non-coplanar breaks (1 to 5) and surrounding resin-rich pockets, with break sites colour-coded by formation load level. (b) XZ view of the Y-axis stack containing the non-coplanar breaks, with four marked positions used to extract cross-sectional XY break planes.

where misplaced fibres are present, as monitored by *in situ* scans. Fig. 1a shows the XZ plane view of the Y-axis stack of Region 1, revealing three misplaced fibres (fibres 1, 2, and 3) in the interply region, with misorientation angles of −26°, 79°, and −35°, respectively. Here, clockwise from the 0° ply axis is defined as the positive direction. These misorientation angles represent the deviation of fibres in the XZ plane relative to the Z-axis loading direction. Fig. 1b shows an XZ slice generated from average projections of aligned fibres, misplaced fibres, and associated breaks within the Region 1 stack at 96 % UTS (see section 2.4). Visual inspection of cross-sectional views of each broken fibre was concurrently performed to establish the correlation of the breaks to the surrounding fibre orientations. The three misplaced fibres appear to cross aligned fibres and come into close contact with them. Fig. 2 shows XY cross-sectional slices at the intersections of the misplaced and aligned fibres. These intersections appear to progressively trigger seven single breaks and one co-planar break pair ('duplet') at load levels up to 96 % UTS, occurring either within the misplaced fibres or in the adjacent aligned fibres. It should be noted that the limited FOV size available in the 150 nm scans allowed the crossings of misplaced fibre 1 with its adjacent fibres to be sufficiently captured, whereas only a smaller portion of misplaced fibres 2 and 3 was captured. Although additional breaks may have occurred outside the scanned region, the breaks identified at the intersections are deemed sufficient to demonstrate the influence of misplaced fibres on break initiation.

3.2. *Break clustering and microscale damage linked to resin-rich pockets within the 0°/0° interply*

A cluster in this study was defined as fibre breaks separated by less than 10 fibre diameters longitudinally (Z-axis) and two fibre diameters radially (X and Y-axis), consistent with the definition used in [25]. Fig. 3b shows the XZ plane view of the Y-axis stack of Region 2, revealing five distinct breaks (1–5) formed on the periphery of resin-rich pockets within the 0°/0° interply. These breaks progressively evolved into a non-coplanar fibre break cluster under increasing load. A non-coplanar cluster of five breaks (1 to 5) and its interactions with surrounding

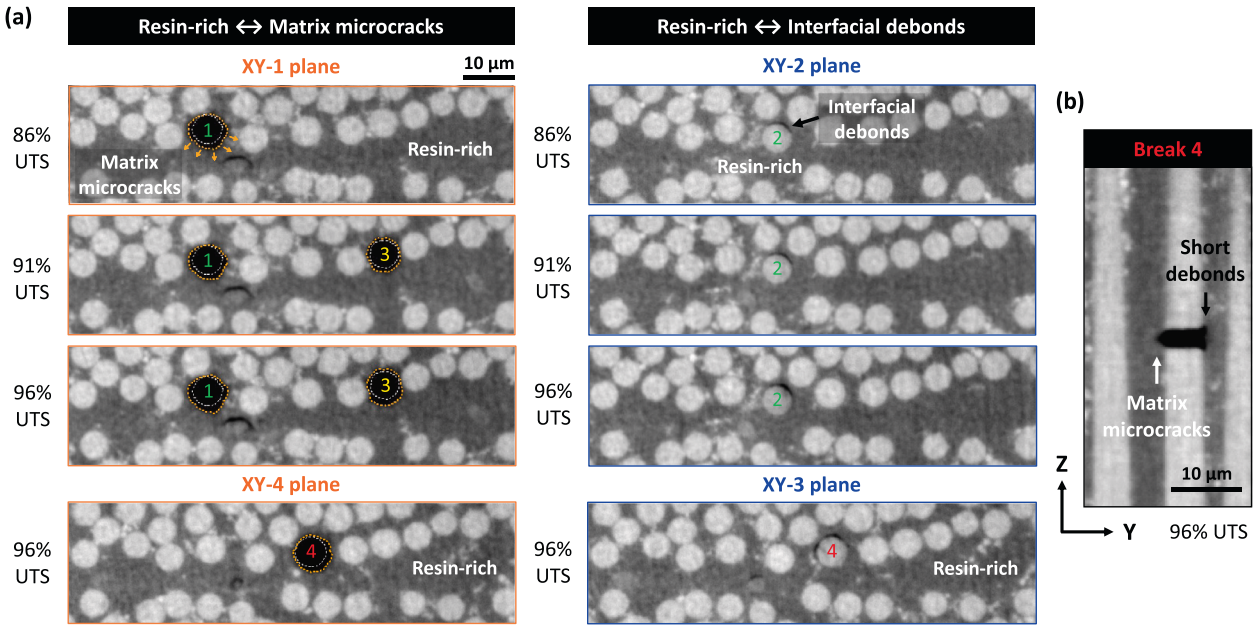

Fig. 4. 150 nm scan; (a) XY break planes of clustered breaks (1 to 4) formed within the Y-stack of Region 2 (Fig. 3), revealing two distinct microscale damage patterns evolving as damage progresses near resin-rich pockets at 86 %, 91 %, and 96 % UTS. XY-1 and XY-4 planes display matrix microcracks propagating non-uniformly toward resin-rich pockets, as indicated by orange arrows. The edges of matrix microcracks and fibres are delineated by orange and white dashed lines, respectively. XY-2 and XY-3 planes show short interfacial debonds originating from break edges that face matrix regions confined by closely packed fibres. (b) YZ break plane at break 4 showing the side-by-side formation of matrix microcracks and short debonds.

resin-rich pockets is analysed at three scan load levels (86 %, 91 %, 96 %). The load level of 67 % UTS was excluded from the analysis due to the absence of breaks in the analysed stack.

In the Y-axis stack at 86 % UTS, breaks 1 and 2 were observed as non-coplanar breaks, with an axial distance of 15 μm between the centre of their respective XY break planes. Fig. 4a shows XY cross-sectional planes of each break, revealing matrix microcracks and short interfacial debonds surrounding the clustered breaks. These two features contrast with their apparent absence around fibre breaks where no resin-rich pockets are present, as reported in [36]. The features, here referred to as 'microcracks' exhibit distinctly blunted crack tips, indicating local inelastic deformation. However, for clarity and consistency, they are referred to as microcracks throughout this study. The XY-1 plane in Fig. 4a shows a matrix microcrack of ~ 1.1 μm in extent adjacent to break 1, propagating toward the adjacent resin-rich pocket and forming an irregular crack configuration around the entire fibre circumference. In the XY-2 plane, asymmetric formation of short interfacial debonds were also observed around break 2 on the side opposite the resin-rich pockets. These debonds, measuring ~ 1.2 μm in axial length along the fibre direction, are limited to the regions where the inter-fibre distance near break 2 is small. At 91 % UTS, break 3 emerged in the vicinity of breaks 1 and 2. While showing no visible debonds, the XY-1 plane of break 3 also reveals matrix microcracks irregularly formed towards the adjacent resin-rich pocket, with an extent of ~ 1.1 μm, similar to those observed near break 1.

In the Y-axis stack at 96 % UTS, additional breaks 4 and 5 appeared in regions of fibres that were likely overloaded by neighbouring breaks 2 and 3. Breaks 4 and 5 were positioned with axial distances of 9 μm from break 2 and 46 μm from break 3, respectively. Overall, this can be seen to form a non-coplanar cluster of five breaks within approximately the same XZ break plane. Break 4 initiated both matrix microcracking and short debonds, consistent with damage patterns seen near resin-rich pockets at lower loads. Fig. 4b shows the orthogonal view of break 4, where the matrix microcracks exhibited relatively wide/blunted crack openings but remained limited in extent to ~ 1.4 μm, with no visible separation of the fibre–matrix interface at the root of the crack. Although only break 4 is presented in orthogonal view in this paper, a similar pattern was consistently observed for all matrix microcracks formed near resin-rich pockets since 86 % UTS. Debonding around break 4 remained consistently confined to the edges of the broken fibre ends, extending to ~ 1.5 μm in length. The extent of the pre-existing matrix microcracks near breaks 1 and 3 increased to ~ 1.5 μm and ~ 1.6 μm, corresponding to increases of ~ 36 % and ~ 45 % relative to their initial formation load step. Similarly, the debonds near break 2 extended to ~ 1.5 μm, representing a ~ 25 % increase.

3.3. *Break clustering and microscale damage linked to larger resin-rich pockets along misoriented fibre groups within the 0° intraply*

Fig. 5a shows the XY plane view of the Y-axis stack of Region 3 from the 150 nm scan, which was examined in a similar manner to sections 3.1 and 3.2. This stack revealed fibre break behaviour associated with three notable features: (i) groups of misoriented fibres, around which larger resin-rich pockets were locally formed compared to other regions, (ii) fibre breaks originating from the intersections of misoriented fibre groups with adjacent fibres, and (iii) a pronounced increase in non-coplanar break clusters within these regions under increasing loads. Comparable break behaviour was also identified in the 650 nm scan, and the corresponding stack, illustrated in Fig. 8, will also be described in the following sections.

3.3.1. *Fibre breaks linked to groups of misoriented fibres (150 nm scan)*

In the Y-axis stack of Region 3, groups of misoriented fibres are distributed across slices from XZ-1 to XZ-5 planes, with their positions at specific XZ planes visualised in Fig. 5a. Fig. 5b presents an example of the misoriented fibres in the XZ plane, showing larger resin-rich pockets originating along regions where misoriented groups of fibres are located. 'Y-stack I', sliced from XZ-1 to XZ-2, is identified to contain the most severely misoriented group of fibres collectively crossing over adjacent aligned fibres with misorientation angles of 8°. The breaks accumulated up to 96 % UTS in Y-stack I are effectively visualised in 2D via average projection in the Y direction. Breaks consistently occur where misoriented fibre groups intersect with adjacent fibres, resembling the break behaviour observed near misplaced fibres (see section

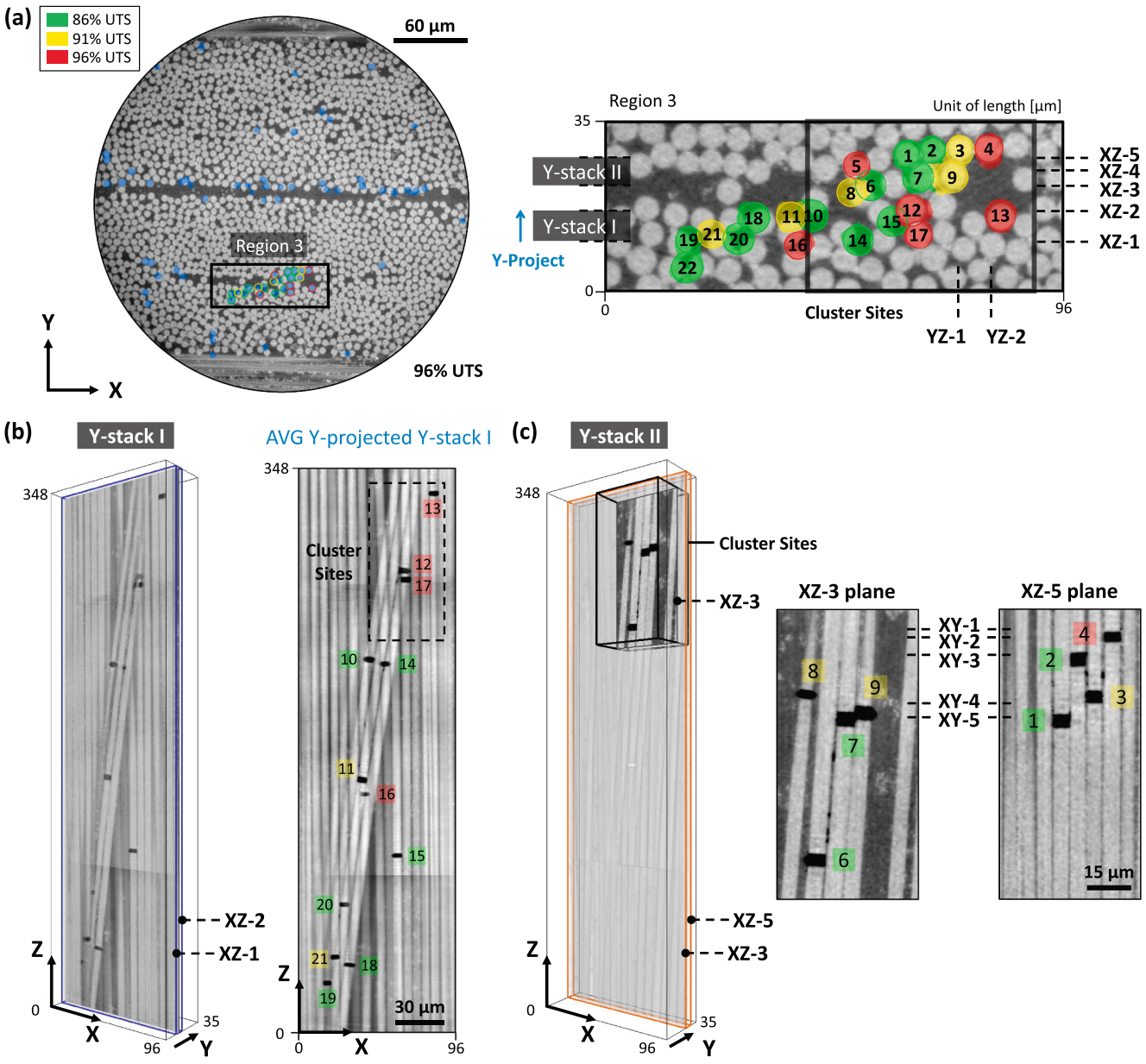

Fig. 5. 150 nm scan; SRCT images showing the fibre breaks interacting with larger resin-rich pockets locally formed along misoriented fibre groups within the 0° intraply region. (a) An XY slice acquired at 96 % UTS within the scan volume containing two 0° plies, showing all breaks within this volume projected as blue dots. The black rectangle at the 0° intraply, labelled as 'Region 3′, marks the cropping region for the Y-axis stack. The magnified XY view of 'Region 3′ shows the projection of breaks (1 to 22) colour-coded by formation load level, highlighting cluster sites where break development was prominent near misoriented fibre groups and larger resin-rich pockets. (b) 'Y-stack I', cropped from the XZ-1 to XZ-2 planes within the Y-axis stack of 'Region 3′, alongside the XZ slice obtained by average projection. (c) 'Y-stack II', cropped from the XZ-3 to XZ-5 planes within the Y-axis stack of 'Region 3′, with magnified XZ break planes showing five marked positions used to extract cross-sectional XY planes.

3.1).

3.3.2. *Fibre breaks linked to groups of misoriented fibres (650 nm scan)*

Fig. 8a presents the XY plane view of the Y-axis stack, obtained from the 650 nm scan, containing misoriented fibre groups and the resulting large resin-rich pockets within the 0° intraply region. A specific region within this stack, spanning slices from XZ-a to XZ-d, was selected for analysis. Fig. 8b shows the XZ plane views of the selected region, illustrating the arrangements of two aligned fibre (AF) bundles and two misaligned fibre (MF) bundles at specific XZ planes. The selected region is further divided into three distinct 'Y-stacks (a to c)' to examine break behaviour under two types of fibre intersection: (i) between AF and MF bundles (Y-stacks a and c), and (ii) between two MF bundles (Y-stack b). The MF 1 and MF 2 bundles are misoriented by 4° and −3° from the 0° ply axis, respectively, with resin-rich pockets prominently distributed in their surrounding regions.

In the Y-stacks (a to c), seven breaks (1 to 5 and 7 to 8) were observed up to 99 % UTS, and their occurrence appears to be related to fibre intersection type (i) or (ii). Fig. 8c shows the 2D visualisation of these breaks, obtained through average projection. In Y-stack b at 89 % UTS, corresponding to type (ii) fibre intersections, break 1 was observed in the MF 2 bundle. The location of break 1 closely matches with the intersection between MF 1 and MF 2 bundles. This break occurrence resembles that previously observed where misplaced fibres and misoriented fibre groups intersect with adjacent fibres, as seen in 150 nm scans, but further extends to cases involving intersections of two

misoriented fibres.

At 94 % UTS, a non-coplanar cluster of three breaks (3, 4, and 5) was detected within Y-stack a, corresponding to type (i) fibre intersections. Breaks 4 and 5, with an axial separation of 36 μm, emerged in the AF 1 bundle at locations where the AF 1 and MF 1 bundles intersected. As another part of the cluster, break 3 was found in the MF 1 bundle immediately adjacent to break 5, with an axial separation of 12 μm. This break site coincided with the location where the MF 1 bundle intersects both the AF 1 and MF 2 bundles, though it remains uncertain which intersection predominantly triggered break 3. Furthermore, the AF 2 bundle within Y-stack c exhibited a type (i) fibre intersection with MF 2 bundle, resulting in break 2. In this case, break 2 progressively formed a co-planar duplet with the pre-existing break 1, exemplifying cluster development reflecting the combined effect of both types (i) and (ii) fibre intersections. At 99 % UTS, the intersections of MF 2 and AF 2 bundles continuously created additional breaks 7 and 8 on either side of the co-planar duplet (1 and 2) along the axial direction. These observed break patterns highlight the role of intersecting fibres, whether type (i) or (ii), in promoting progressive break development.

3.3.3. Break clustering and microscale damage linked to larger resin-rich pockets (150 nm scan)

Fig. 5c presents 'Y-stack II', spanning the XZ-3 to XZ-5 planes within the Region 3 stack from the 150 nm scan. A specific region within Y-stack II, labelled with black rectangles and referred to as the cluster sites, was selected for analysis. The cluster sites contained non-coplanar breaks located near resin-rich pockets locally formed along misoriented fibre groups, where most of the breaks predominantly develop within the same XZ break planes. These breaks are visualised in 2D slices taken at the XZ-3 and XZ-5 planes of the cluster sites at 96 % UTS.

At 86 % UTS, two pairs of non-coplanar breaks were observed within the cluster sites: breaks 6 and 7 in the XZ-3 plane, and breaks 1 and 2 in the XZ-5 plane. These two pairs of clustered breaks were separated axially by 48 μm and 21 μm, respectively. Larger resin-rich pockets are clearly visible around the site of break 6 and 7, induced by misoriented fibre groups in the XZ-3 plane. These misoriented groups are also in contact with other misoriented fibres reported earlier in Y-stack I. Breaks 7 and 1, part of the clusters, share the same XY-5 break plane in the fibre cross-section and are located immediately adjacent to each other, forming a co-planar duplet. Figs. 6a and c show the XZ-4 and XZ-5 plane views of this co-planar duplet, revealing matrix microcracks and short interfacial debonds initiated at breaks 7 and 1, respectively. Their damage patterns and configuration appear similar to those observed around breaks located near resin-rich pockets.

At 91 % UTS, three additional breaks were detected in close proximity to the non-coplanar clusters formed in the XZ-3 and XZ-5 planes at 86 % UTS: a single break 8 and a non-coplanar duplet (9 and 3). In this case, the focus of observation was on breaks 9 and 3, with their break sites immediately adjacent to the pre-existing co-planar duplet (7 and 1) and non-coplanar breaks (1 and 2). The YZ-1 and XZ-4 planes in Figs. 6b and c show that breaks 9 and 3 form with an axial separation of 5 μm, while break 9 lay nearly in the same cross-sectional plane as break 7. Interestingly, the XZ-4 plane reveals two apparent features on either side of break 9. The right side of break 9, where resin-rich pockets are present, exhibited non-uniform matrix microcracks propagating toward the resin-rich pockets, consistent with those observed at 86 % UTS. Damage features, appearing as microvoids or the onset of matrix microcracks, were visible on the upper right and left sides of break 9, particularly in

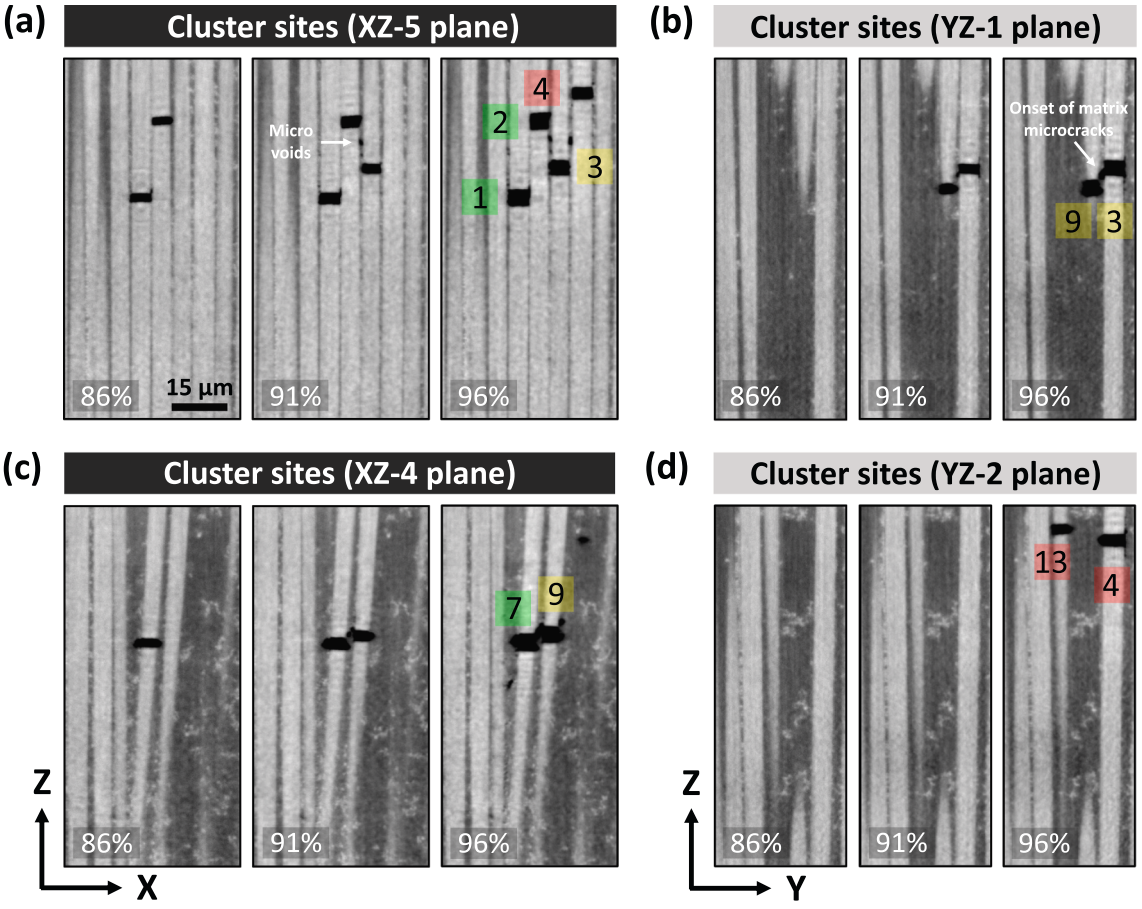

Fig. 6. 150 nm scan; XZ and YZ views of cluster sites in 'Y-stack II' at (a) XZ-5, (b) YZ-1, (c) XZ-4, and (d) YZ-2 planes, showing non-coplanar breaks with associated microscale damage at 86 %, 91 %, and 96 % UTS.

the inter-fibre matrix region between breaks 7 and 9, though their exact nature remains uncertain. It should be noted that these damage features were absent in the scans taken at lower loads, suggesting that their formation is associated with the surrounding break behaviour. Similar damage features were also detected at break 3, positioned next to break 2 in the XZ-5 plane, which was axially separated by 13 μm, and resin-rich pockets extending toward break 9 in the YZ-1 plane. Microvoids, shown in the XZ-5 plane, appear to form within the inter-fibre matrix region between breaks 2 and 3, where stress interactions between the breaks are expected to occur. The lower left side of break 3 in the YZ-1 plane shows damage resembling the onset of matrix microcracks within the inter-fibre matrix region between break 9 and 3, facing the resin-rich pockets. A highly localised short debond was additionally detected on the right side of the interface of break 3.

With further loading to 96 % UTS, two single breaks, 4 and 13, were detected in fibres facing the large resin-rich pockets, with break 4 forming immediately next to the pre-existing non-coplanar cluster (1 to 3) in the XZ-5 plane. The location of break 4 was axially separated by 21 μm from break 3, which may then be identified as a non-coplanar cluster (1 to 3). Interestingly, new microvoid formation was also detected within the inter-fibre matrix region between breaks 4 and 3, as observed at 91 % UTS. The YZ-2 plane in Fig. 6d shows that similar matrix microcracking patterns persist in both breaks 4 and 13, with short interfacial debonds visible on the right side of break 4. Moreover, the pre-existing non-coplanar clusters (9 and 3) and (7 and 9), shown in Figs. 6b and c, opened further, with the surrounding earlier-formed damage continuing to evolve. As revealed by the XZ-5 and YZ-1 planes, the previously reported damage features (i.e. microvoids or onset of matrix cracks) within the inter-fibre matrix region grew in size and eventually linked with adjacent breaks previously unlinked at earlier loads. Accompanying this damage progression, significant propagation of matrix microcracks was also detected along the inter-fibre matrix regions of the pre-existing clustered breaks (9 and 3), (7 and 9), and (7 and 1).

Fig. 7 presents the XY planes of these breaks at 96 % UTS, showing matrix microcracks at their maximum propagation in the cross-sectional view. Break 3 in the XY-4 plane shows matrix microcracks prominently propagating across the inter-fibre matrix region toward the fibre where break 9 occurred, located near the large resin-rich pockets. A similar matrix microcrack propagation behaviour was observed in the inter-fibre matrix region between breaks 7 and 9 in the XY-5 plane. Accordingly, the matrix microcracks propagating from break 3 appear to connect with those surrounding clustered breaks 9, 7, and 1, forming a continuous damage zone.

4. Discussion – Roles of local microstructural variations on fibre break development

4.1. Role of misplaced fibres in break initiation

Building on the fibre breaks observed in regions with misplaced fibres (see section 3.1), we propose two hypotheses to explain the mechanisms underlying this break behaviour. In the first instance, it may be argued that the formation of multiple breaks at the intersections between misplaced and aligned fibres might be related to the tow spreading and resin impregnation process during prepreg manufacturing. These two processes, when conducted through the direct contact (mechanical) method, employ a series of spreading or impregnation rollers to flatten the fibre tows into a uniform prepreg sheet. As the fibre tows pass through the rollers, the fibres on the surface of a ply come into contact with them during the processing. Moradi *et al.* [49] indicate that shear and frictional stresses can build up on the fibre tows due to their contact with the rollers. It is arguable that these stresses could concentrate on misplaced and misaligned fibre tows crossing over aligned fibres on the ply surface, potentially leading to excessive fibre abrasion and damage to the filaments constituting the fibre tows. This in turn could introduce strength controlling-defects at the crossing points. Consequently, we hypothesise that this could explain the increased prevalence of fibre breaks within the interply region, where misplaced fibres intersect with aligned fibres. Similarly, Mesquita *et al.* [50] reported a higher occurrence of fibre breaks closer to the ply interface in thin plies, in the absence of strongly misaligned fibres. This study suggested that fibre weakening introduced during the tow spreading process served as a damage precursor to this breaking behaviour, consistent

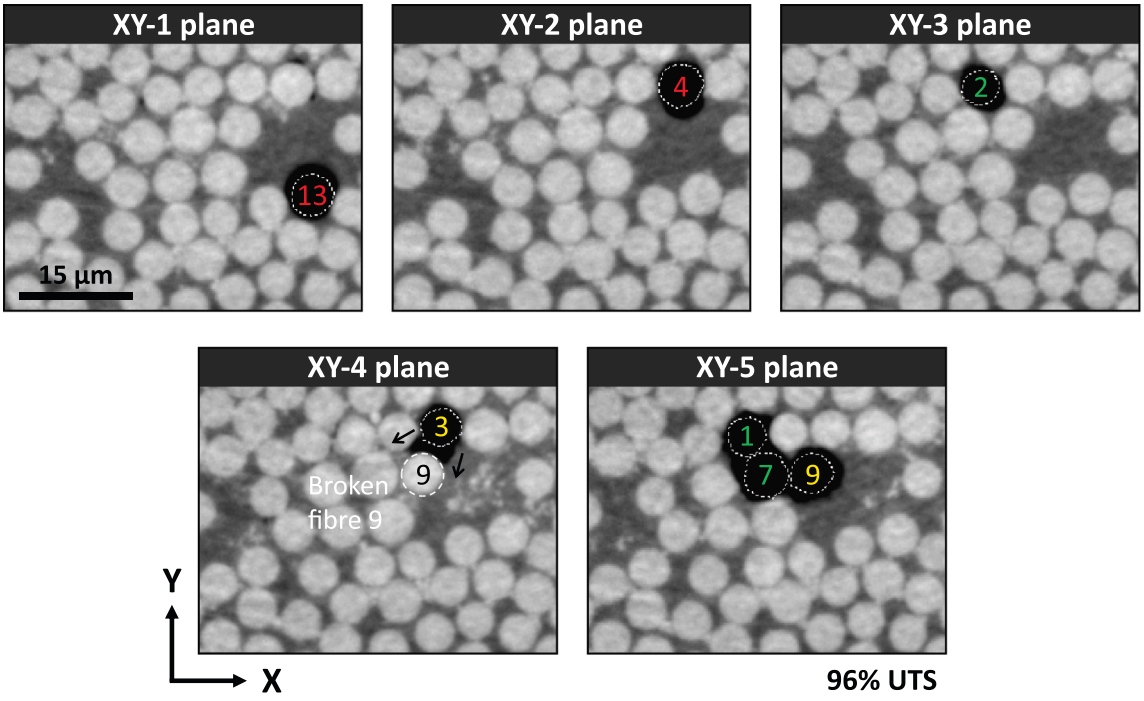

Fig. 7. 150 nm scan; Cross-sectional XY views of non-coplanar breaks at 96 % UTS, taken from cluster sites in 'Y-stack II' at XY-1 to XY-5 planes, showing extensive propagation of matrix microcracks linking (black arrows) breaks 1, 3, 7, and 9 formed at 86 % and 91 % UTS.

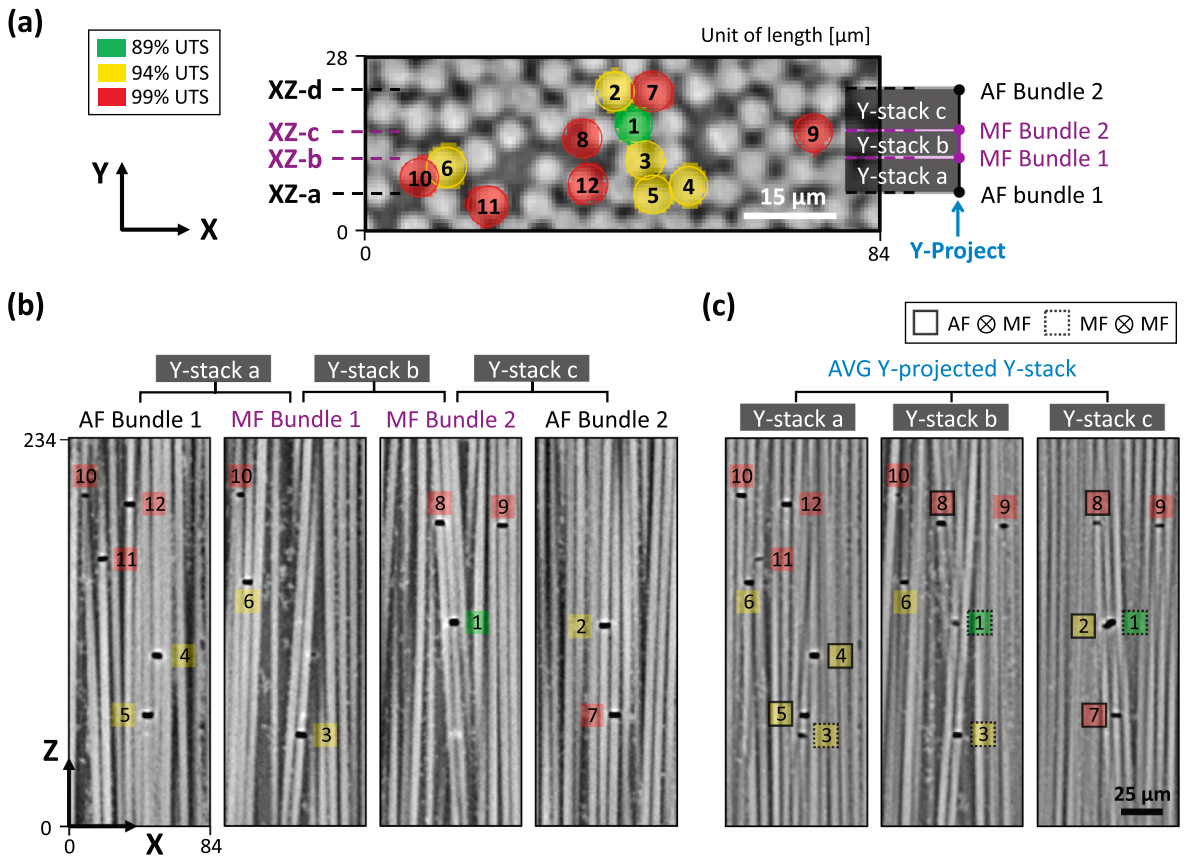

Fig. 8. 650 nm scan; SRCT images showing the fibre breaks interacting with groups of misoriented fibres within the 0° intraply region. (a) An XY view of the analysed stack, taken from the scan volume containing four 0° plies at 99 % UTS, showing the projection of breaks (1 to 12) colour-coded by their formation load levels of 89 %, 94 %, and 99 % UTS. Three sub-stacks, 'Y-stacks a, b, and c', were cropped from the analysed stack across the XZ-a to XZ-d planes, with their locations marked. (b) XZ views of three Y-stacks containing aligned fibre (AF) and misoriented fibre (MF) bundles, showing fibre breaks within AF or MF bundles. (c) XZ slices obtained via average projection of each Y-stack along the Y-axis, showing seven break sites at intersections between AF and MF bundles (denoted as ⊗): AF ⊗ MF (solid lines) or MF ⊗ MF (dashed lines).

with the hypothesis we propose.

A further potential explanation for the observed fibre break behaviour could be micro-mechanical influences from the local fibre misalignments, particularly local stress concentrations arising at intersections of misplaced and adjacent fibres. When fibre bundles are loaded in tension, misplaced fibres with high misorientation angles can significantly disrupt the uniform load redistribution between the fibre and matrix. The loaded misplaced fibres themselves may experience bending stresses in addition to axial stresses, placing them in a multi-axial stress state. Accordingly, this may induce higher shear stresses in the matrix surrounding the misplaced fibres, leading to the formation of inhomogeneous stress states in nearby fibres [12]. As the misplaced fibres cross over adjacent aligned fibres, local stress concentrations are likely to be further intensified at their intersections. Consequently, this could impart elevated stresses to misplaced or aligned fibres, or both, increasing their susceptibility to failure.

Fig. 2 shows breaks (1 to 9) located immediately adjacent to or within misplaced fibres, exemplifying the strong influence of micro-mechanical effects at intersections. Notably, the formation of co-planar breaks (4 and 5) was also observed as early as at 67 % UTS, when two misplaced fibres 1 and 2 crossed and contacted adjacent aligned fibres. This phenomenon could be attributed to intensified local stress concentrations caused by crossing of these two misplaced fibres under load. These crossings tend to reduce inter-fibre distances, which are likely to elevate stress concentrations on the surface of adjacent fibres and promote co-planar breaks, consistent with findings by Yamamoto *et al.* [9]. Overall, the occurrence of breaks (1 to 9) linked to misplaced fibres is explained by two proposed mechanisms. Although both mechanisms are not mutually exclusive and may act concurrently, their individual contributions remain uncertain.

4.2. *Role of resin-rich pockets in break clustering and microscale damage development*

While the root cause of the thicker and wider resin-rich pockets is beyond the core scope of this work, it may initially be linked to imperfect tow spreading process during prepreg manufacturing. This process can result in uneven fibre distribution (i.e., fibre misalignment) including gaps between fibre bundles and regions with fewer or no fibres. These fibre-sparse regions are filled with excess resin during resin impregnation process, consequently forming resin-rich pockets. The fibre arrangements shown in Fig. 3b prominently exemplify the significant impact of uneven fibre distribution on resin-rich pocket formation. In addition, the Y-axis stack of Region 2 is contained within that of Region 1 in the interply region, where fibres near resin-rich pockets lie adjacent to three misplaced fibres. This indicates that the fibres may have experienced disrupted fibre distribution and altered resin flow during prepreg manufacturing, likely influenced by the neighbouring misplaced fibres. For instance, during the consolidation of two adjacent 0° plies across this interply region, resin may have preferentially redistributed into gaps between unevenly distributed fibres. This could potentially explain the non-uniformly increased interlaminar thickness observed in their immediate vicinity.

Fig. 3b presents the sequential development of a non-coplanar cluster of five breaks (1 to 5), initiated by non-coplanar breaks (1 and 2), within the same XZ break plane in contact with resin-rich pockets.

This progressive clustering suggests an interaction with resin-rich pockets, which is characterised by two microscale damage patterns: non-uniform matrix microcracks and short interfacial debonds (see Fig. 4**)**. Across all load levels, these two damage patterns tend to appear side by side surrounding the broken fibre but develop in distinct locations.

Firstly, matrix microcracks form at break edges facing resin-rich pockets and extend into these regions, with their non-uniform configuration growing in size as the load increases. This tendency may be consistent with the relatively low local stiffness in resin-rich areas adjacent to the broken fibre, where fewer fibres are present to suppress crack development, permitting greater crack opening [18]. Interestingly, despite the wide opening of the cracks, the maximum extent of crack propagation is relatively short (~1.6 μm), considerably lower than the matrix crack sizes reported in previous research [20,51]. Such cracking behaviour could be linked to locally occurring shear nonlinearity in the matrix near resin-rich pockets. Yang *et al.* [52] suggest that shear nonlinearity in carbon epoxy composites may originate from a microscale processes such as craze formation. In addition, molecular-level plasticity in the resin is reported as a potential source of shear nonlinearity, even in small regions of the matrix. In light of these findings, the most plausible explanation for the observed matrix microcracks is that higher stress concentrations adjacent to breaks drive localised plastic deformation in resin-rich regions with lower local stiffness, and the resulting shear nonlinearity determines the degree of crack blunting as opposed to propagation.

In contrast, short interfacial debonds initiate at break edges further from resin-rich pockets, where the surrounding matrix regions are confined by fibres with smaller inter-fibre distances. Although the debonds extend slightly with increasing loads, their propagation remains highly localised near the break edges, reaching no further than ~ 1.5 μm. This debonding configuration may be attributed to the localisation of shear stresses induced by breaks. The resulting shear stresses in the matrix likely concentrate more in regions with smaller inter-fibre distances than those near resin-rich pockets, potentially exceeding the shear strength of the matrix and the interfacial shear strength. From an energy standpoint, the short extent of the debonds suggests that the strain energy released from a fibre break was not favourably absorbed through debonding. Rather, a greater portion of the energy was likely absorbed by matrix cracking and matrix plasticity, as discussed above. As shown in Fig. 4b, the side-by-side formation of debonds and matrix microcracks around the same fibre break suggests that the driving forces and resistance for these two damage patterns are closely balanced in this material system. The competition between them in damage formation may be an important consideration for future materials development and modelling of failure processes.

The continuous formation and development of matrix microcracks and debonds at loads above 86 % UTS suggests that breaks near resin-rich pockets are likely to induce more localised stress concentrations in the matrix and interface while reducing the effective matrix stiffness and introducing shear nonlinearity. As a result, load transfer between fibres could be exacerbated, overloading intact fibres near both newly formed and pre-existing breaks at each load level. This could increase the likelihood of cascading effects that promote the clustering of breaks under increasing loads, which may explain how resin-rich pockets drive the formation of non-coplanar clusters within the interply region. Another factor contributing to the cluster development could be the increased prevalence of breaks at or near the ply interface. Consistent with the first hypothesis on breaks near misplaced fibres (see section 4.1), a plausible assumption is that the fibres in which clustered breaks (1 to 5) formed may have been relatively weak, possibly due to surface damage induced during the tow spreading process.

4.3. Role of misoriented fibre groups and larger resin-rich pockets in break clustering and microscale damage development

Fibre bundles, observed separately in the 150 nm (Fig. 5b) and 650 nm scans (Fig. 8b), consistently exhibit break initiation at the intersections between groups of misoriented fibres and adjacent fibres (see section 3.3), closely resembling the break behaviour seen near misplaced fibres (see section 3.1). As such, we propose that micro-mechanical effects, i.e. local stress concentrations arising at the intersections, could explain this break behaviour, consistent with the hypothesis proposed on breaks linked to misplaced fibres. Furthermore, Jafarypouria *et al.* [22] demonstrated the significant influence of fibre misalignment on stress concentrations in fibre bundles using microscale UD fibre models. However, it should be noted that their study employed different parameters, including glass fibres, smaller fibre misalignment angles (1.4° to 5°), and a different arrangement of misaligned fibre bundles. Nevertheless, their study reported two key findings that can further support our interpretation. First, at a fibre volume fraction of 50 %, peak stress concentration factors in the neighbouring intact fibres surrounding a break were ~ 33 % higher in misaligned fibre bundles than in perfectly aligned ones. Second, stress concentrations in misaligned fibre bundles become increasingly localised with increasing fibre volume fraction, suggesting that the influence of misalignment intensifies as the inter-fibre distance between broken and intact fibres decreases.

In particular, Y-stack II shown in Fig. 5c highlights break clustering near large resin-rich pockets, where initial breaks in groups of misoriented fibres progressively evolve into either co-planar or non-coplanar breaks. Together with micro-mechanical effects, we propose a tentative hypothesis that could explain the clustering behaviour. Stress redistribution from a broken fibre to its neighbouring intact fibres may have been hindered by the combined effects of fibre misalignment, large resin-rich pockets, and matrix non-linearity, intensifying overload effects on neighbours and promoting cluster development. Another finding by Jafarypouria *et al.* [22] supports this hypothesis, showing that misaligned fibres surrounding a break exhibit higher levels of SCFs at the closest distance to the broken fibre compared to aligned fibres. This effect becomes more pronounced with increasing fibre volume fraction (i.e., smaller inter-fibre distance to the broken fibre). Additionally, SCFs in misaligned fibres around a break decay to zero more slowly with distance from the break under 2 % strain, where the matrix undergoes nonlinear deformation, compared to 0.1 % strain, where only elastic deformation occurs. This suggests a larger overload effect on neighbouring intact fibres, particularly when fibre misalignment and matrix nonlinearity co-occur, potentially increasing their susceptibility to failure.

Moreover, Fig. 6 and Fig. 7 highlight that clustered breaks in Y stack II are consistently accompanied by matrix microcracks, short interfacial debonds, and microvoids. These damage features, as discussed in section 4.2, provide evidence of severe matrix nonlinearity in these break regions. Notably, Fig. 7 illustrates that the propagation of matrix microcracks in Y-stack II expands with increasing load, progressively linking pre-existing clustered breaks through the inter-fibre region. This underscores the severity of matrix nonlinearity, particularly when break sites are influenced by both fibre misalignment and the resulting resin-rich pockets. Furthermore, Swolfs *et al.* [17] reported that the tips of matrix cracks may induce very high stress gradients across fibres. If so, these gradients could play an additional role in intensifying matrix nonlinearity.

Since stress redistribution around these clustered breaks has not been quantified in the current study, the extent to which the combined effects of fibre misalignment, large resin-rich pockets, and matrix non-linearity influence stress redistribution remains uncertain. Nevertheless, these combined effects, in conjunction with the aforementioned micro-mechanical effects, provide a compelling explanation for the characteristic clustering behaviour and associated damage patterns.

5. Conclusions

This study investigates the interaction between local microstructural variations and fibre breaks in 0° carbon fibre plies, exploring how these interactions contribute to the clustering of breaks. *In situ* tensile tests, combined with 150 nm-based X-ray synchrotron holotomography, were conducted to monitor the accumulation of breaks in regions with microstructural variations at different stress levels, reaching up to 96 % of their ultimate strength. Three distinctive microstructures are identified which drive a pronounced increase in single and clustered breaks: misplaced fibres and resin-rich pockets within the 0°/0° interply region, and large resin-rich pockets formed locally around misoriented fibre groups within the 0° intraply region.

First, three misplaced fibres within the interply region are observed intersecting multiple adjacent fibres with significant misalignment. These intersections coincide with locations where multiple single breaks and one co-planar break formed, either within the misplaced fibres or the adjacent fibres. The observed break behaviour was explained by two hypotheses: (1) increased prevalence of breaks at the ply interface, promoted by fibre damage introduced during the tow spreading and impregnation process, and (2) local stress concentrations induced by misplaced fibres at intersections.

Second, resin-rich pockets within the interply region are identified to influence the progressive development of a non-coplanar cluster of five breaks. The clusters are also characterised by two distinct microscale damage patterns: non-uniform matrix microcracks and short interfacial debonds. The matrix microcracks initiate at break edges facing resin-rich pockets and propagate locally into these regions, forming an irregular crack configuration. This cracking behaviour was explained by the lower local stiffness in resin-rich pockets and matrix nonlinearity driven by local plastic deformation. In contrast, short debonds originate at break edges facing matrix regions confined by closely packed fibres. Their propagation remains limited, explained by two mechanisms: (1) localisation of shear stresses in the matrix, and (2) the less favourable dissipation of strain energy through debonding.

Third, larger resin-rich pockets formed locally along groups of misoriented fibres are identified to promote the progressive clustering of breaks formed within misoriented fibres. Consistent with the microscale damage observed earlier, the clustered breaks are also accompanied by the simultaneous formation of matrix microcracks and short interfacial debonds, along with features appearing as microvoids or the onset of matrix microcracks. The resulting damage is indicative of matrix shear nonlinearity, strongly supporting the occurrence of severe matrix nonlinearity in these break regions. Another characteristic break behaviour is the progressive formation of breaks at intersections between the most severely misoriented fibre groups and adjacent fibres. This break behaviour largely aligns with that observed near misplaced fibres, further supporting our earlier hypothesis on intensified local stress concentrations at intersections.

While addressing the two key research questions (see section 1), this study helps bridge the gap in the previously reported understanding of how local microstructural variations influence longitudinal tensile failure by *in situ* monitoring their actual response to fibre breaks via 150 nm-based holotomography. The identified break patterns, clustering behaviour, and resulting microscale damage shed new light on the importance of considering their critical role in fibre break development for more reliable predictions of longitudinal tensile failure. Future work could focus on developing fibre break models that incorporate the microstructural variations identified in this study, such as misplaced or misoriented fibre groups intersecting aligned fibres and larger resin-rich pockets. In addition to quantitatively verifying the hypotheses proposed in this study, this would help determine the extent to which these microstructural variations influence local stress concentrations and diminish stress redistribution around breaks. The SRCT volumes analysed in this study are publicly available in a Zenodo dataset [53] for further analysis by other researchers.

CRediT authorship contribution statement

Yeajin Lee: Writing – original draft, Visualization, Methodology, Investigation, Conceptualization. **Thanasis Chatziathanasiou:** Writing – review & editing, Methodology, Investigation, Conceptualization. **Christian Breite:** Writing – review & editing, Methodology, Investigation, Conceptualization. **Mahoor Mehdikhani:** Writing – review & editing, Methodology, Investigation, Conceptualization. **Yentl Swolfs:** Writing – review & editing, Methodology, Investigation, Conceptualization. **Mark N. Mavrogordato:** Writing – review & editing, Supervision, Methodology, Conceptualization. **S. Mark Spearing:** Writing – review & editing, Supervision, Methodology, Conceptualization. **Ian Sinclair:** Writing – review & editing, Supervision, Methodology, Funding acquisition, Conceptualization.

Declaration of competing interest

The authors declare that they have no known competing financial interests or personal relationships that could have appeared to influence the work reported in this paper.

Acknowledgement

The authors would like to acknowledge the contributions from the Mitsubishi Chemical Corporation (Advanced Molding and Composites Laboratory, Aichi R&D centre, Japan) and the dedicated MCC scientists – Fukuhara Yasuhiro, Takano Tsuneo, Sugiura Naoki – for their sponsorship, material supplies, and technical support. The work leading to this publication was supported by the Engineering and Physical Sciences Research Council (EP/W003333/1). The authors would also like to acknowledge the KU Leuven Research Council for project C14/21/076 and the Research Foundation Flanders for the postdoctoral fellowships ToughImage (126342IN), BIOPTOUGH (12B0624N), and COCOMI (1231322 N).

The authors acknowledge the European Synchrotron Radiation Facility (ESRF) for the provision of synchrotron radiation facilities at the ID16B and ID19 beamline under proposal number MA5729 and MA5711, respectively. We greatly appreciate the technical support and insightful advice provided by the beamline scientists at ID16B (Julie Villanova and Olga Stamati) and ID19 (Partha Paul and Ludovic Broche) throughout the preparation and execution of the experiments, as well as the reconstruction of the scans. We also extend deepest gratitude to our colleagues in the MA5729 experiment (Sina AhmadvashAghbash, Babak Fazlali) and MA5711 experiment (Fernando Alvarez-Borges, Orestis Katsamenis, Marco Endrizzi, Lorenzo Massimi, Fabio De Marco, Vittorio Di Trapani) for invaluable assistance and insightful advice in performing *in situ* SRCT experiments.

The μ-VIS X-Ray Imaging Centre at the University of Southampton is acknowledged for the 3D image acquisition and post-processing tools. Credit is further extended to the technicians at the Engineering Design and Manufacturing Centre (EDMC) at the University of Southampton (Simon Beever, Steven Jenkinson, and Amelia Ellis) for their technical supports in preparing the specimens through water-jet cutting.

Data availability

The authors have made the SRCT data publicly available in Zenodo, and this is clearly stated in the manuscript. Link: https://zenodo.org/records/17099577.

References

[1] Swolfs Y, Verpoest I, Gorbatikh L. A review of input data and modelling assumptions in longitudinal strength models for unidirectional fibre-reinforced composites. Compos Struct 2016;150:153–72.
[2] Weibull W. A statistical distribution function of wide applicability. J Appl Mech 1951.

[3] Watanabe J, Tanaka F, Okuda H, Okabe T. Tensile strength distribution of carbon fibers at short gauge lengths. Adv Compos Mater 2014;23(5–6):535–50.
[4] Hedgepeth JM, Van Dyke P. Local stress concentrations in imperfect filamentary composite materials. J Compos Mater 1967;1(3):294–309.
[5] Hedgepeth JM. Stress concentrations in filamentary structures. National Aeronautics and Space Administration 1961.
[6] Fukuda H. Stress concentration factors in unidirectional composites with random fiber spacing. Compos Sci Technol 1985;22(2):153–63.
[7] Xia Z, Curtin W, Okabe T. Green's function vs. shear-lag models of damage and failure in fiber composites. Compos Sci Technol 2002;62(10–11):1279–88.
[8] Xia Z, Okabe T, Curtin WA. Shear-lag versus finite element models for stress transfer in fiber-reinforced composites. Compos Sci Technol 2002;62(9):1141–9.
[9] Yamamoto G, Onodera M, Koizumi K, Watanabe J, Okuda H, Tanaka F, et al. Considering the stress concentration of fiber surfaces in the prediction of the tensile strength of unidirectional carbon fiber-reinforced plastic composites. Compos A Appl Sci Manuf 2019;121:499–509.
[10] Watanabe J, Tanaka F, Higuchi R, Matsutani H, Okuda H, Okabe T. A study of stress concentrations around fiber breaks in unidirectional CF/epoxy composites using double-fiber fragmentation tests. Adv Compos Mater 2018;27(6):575–87.
[11] Yamamoto G, Oshima K, Ramadhan RA, Lim T, Megra YT, Suk JW, et al. Tensile strength prediction of unidirectional polyacrylonitrile (PAN)-based carbon fiber reinforced plastic composites considering stress distribution around fiber break points. Compos A Appl Sci Manuf 2024;183:108234.
[12] Breite C. Aligning Fibre break Models for Composites with the Observable Micro-scale Material Behaviour (PhD Thesis). KU Leuven 2021.
[13] Lomov SV, Breite C, Melnikov A, Mesquita F, Swolfs Y, Abaimov SG. Clusters and avalanches of fibre breaks in a model of an impregnated unidirectional fibre bundle under tension. Int J Solids Struct 2021;225.
[14] Smith R, Phoenix S, Greenfield M, Henstenburg R, Pitt R. Lower-tail approximations for the probability of failure of three-dimensional fibrous composites with hexagonal geometry. Proc R Soc Lond A Math Phys Sci 1983;388 (1795):353–91. https://royalsocietypublishing.org/doi/10.1098/rspa.1983.0087.
[15] Cox H. The elasticity and strength of paper and other fibrous materials. Br J Appl Phys 1952;3(3):72.
[16] Nedele MR, Wisnom MR. Three-dimensional finite element analysis of the stress concentration at a single fibre break. Compos Sci Technol 1994;51(4):517–24.
[17] Swolfs Y, Morton H, Scott AE, Gorbatikh L, Reed PAS, Sinclair I, et al. Synchrotron radiation computed tomography for experimental validation of a tensile strength model for unidirectional fibre-reinforced composites. Compos Part a-Appl S 2015; 77:106–13.
[18] Swolfs Y, Gorbatikh L, Romanov V, Orlova S, Lomov SV, Verpoest I. Stress concentrations in an impregnated fibre bundle with random fibre packing. Compos Sci Technol 2013;74:113–20.
[19] AhmadvashAghbash S, Breite C, Mehdikhani M, Swolfs Y. Longitudinal debonding in unidirectional fibre-reinforced composites: Numerical analysis of the effect of interfacial properties. Compos Sci Technol 2022;218.
[20] AhmadvashAghbash S, Fazlali B, Mehdikhani M, Swolfs Y. Finite element analysis of the effect of longitudinal debonding on stress redistributions around fibre breaks in randomly packed fibres. Compos Sci Technol 2022;227.
[21] Smith RL. The Random Variation of Stress-Concentration Factors in Fibrous Composites. J Mater Sci Lett 1983;2(8):385–7.
[22] Jafarypouria M, Lomov SV, Mahato B, Abaimov SG. The effect of fibre misalignment in an impregnated fibre bundle on stress concentrations. Compos Part a-Appl S 2024;178.
[23] AhmadvashAghbash S, Verpoest I, Swolfs Y, Mehdikhani M. Methods and models for fibre–matrix interface characterisation in fibre-reinforced polymers: a review. Int Mater Rev 2023;68(8):1245–319.
[24] Scott AE, Sinclair I, Spearing SM, Thionnet A, Bunsell AR. Damage accumulation in a carbon/epoxy composite: Comparison between a multiscale model and computed tomography experimental results. Compos Part a-Appl S 2012;43(9):1514–22.
[25] Schöberl E, Breite C, Melnikov A, Swolfs Y, Mavrogordato MN, Sinclair I, et al. Fibre-direction strain measurement in a composite ply under quasi-static tensile loading using Digital volume Correlation and in situ Synchrotron Radiation Computed Tomography. Compos A Appl Sci Manuf 2020;137:105935.
[26] Withers PJ, Bouman C, Carmignato S, Cnudde V, Grimaldi D, Hagen CK, et al. X-ray computed tomography. Nat Rev Methods Primers 2021;1(1):18.
[27] Fast T, Scott A, Bale H, Cox B. Topological and Euclidean metrics reveal spatially nonuniform structure in the entanglement of stochastic fiber bundles. J Mater Sci 2015;50:2370–98.
[28] Emerson MJ, Jespersen KM, Dahl AB, Conradsen K, Mikkelsen LP. Individual fibre segmentation from 3D X-ray computed tomography for characterising the fibre orientation in unidirectional composite materials. Compos A Appl Sci Manuf 2017; 97:83–92.
[29] Rosini S, Mavrogordato MN, Egorova O, Matthews ES, Jackson SE, Spearing SM, et al. In situ statistical measurement of local morphology in carbon-epoxy composites using synchrotron X-ray computed tomography. Compos Part a-Appl S 2019;125.
[30] Fritz NK, Kopp R, Nason AK, Ni XC, Lee J, Stein IY, et al. New interlaminar features and void distributions in advanced aerospace-grade composites revealed via automated algorithms using micro-computed tomography. Compos Sci Technol 2020;193.
[31] Malgioglio F, Pimenta S, Matveeva A, Farkas L, Desmet W, Lomov SV, et al. Microscale material variability and its effect on longitudinal tensile failure of unidirectional carbon fibre composites. Compos Struct 2021;261:113300.
[32] Bull D, Helfen L, Sinclair I, Spearing S, Baumbach T. A comparison of multi-scale 3D X-ray tomographic inspection techniques for assessing carbon fibre composite impact damage. Compos Sci Technol 2013;75:55–61.
[33] Garcea S, Wang Y, Withers P. X-ray computed tomography of polymer composites. Compos Sci Technol 2018;156:305–19.
[34] Morton H. 3D imaging of the tensile failure mechanisms of carbon fibre composites. University of Southampton; 2014.
[35] Scott A, Mavrogordato M, Wright P, Sinclair I, Spearing S. In situ fibre fracture measurement in carbon–epoxy laminates using high resolution computed tomography. Compos Sci Technol 2011;71(12):1471–7.
[36] Chatziathanasiou T, Lee Y, Villanova J, Stamati O, Ahmadvashaghbash S, Fazlali B, et al. Questioning the Representativeness of damage Mechanisms in Single-Fiber Composites via In Situ Synchrotron X-Ray Holo-Tomography. Small 2024.
[37] Chatziathanasiou T, Breite C, Diehl M, Mehdikhani M, Swolfs Y. In situ transverse single-fibre and bundle tests in synchrotron nano-tomography to unravel interfacial debonding in carbon and glass fibre-epoxy composites. Composites Part A: Applied Science and Manufacturing; 2025.
[38] Schöberl E, Breite C, Rosini S, Swolfs Y, Mavrogordato M, Sinclair I, et al. A novel particle-filled carbon-fibre reinforced polymer model composite tailored for the application of digital volume correlation and computed tomography. J Compos Mater 2021;55(14):1907–34.
[39] Mehdikhani M, Breite C, Swolfs Y, Soete J, Wevers M, Lomov SV, et al. Digital volume correlation for meso/micro in-situ damage analysis in carbon fiber reinforced composites. Compos Sci Technol 2021;213:108944.
[40] Chatziathanasiou T, Demir O, Soete J, Breite C, Mehdikhani M, Diehl M, et al. Material representativeness of a polymer matrix doped with nanoparticles as the random speckle pattern for digital volume correlation of fibre-reinforced composites. Compos B Eng 2024;276:111381.
[41] Wright P, Moffat A, Sinclair I, Spearing S. High resolution tomographic imaging and modelling of notch tip damage in a laminated composite. Compos Sci Technol 2010;70(10):1444–52.
[42] 3M™, Data Sheets- 3M Scotch-Weld™ Structural Epoxy Adhesive EC-9323 B/A, 2021. https://multimedia.3m.com/mws/media/2157921O/3m-ec-9323-ba-structural-epoxy-paste-adhesive-tds.pdf.
[43] Martínez-Criado G, Villanova J, Tucoulou R, Salomon D, Suuronen J-P, Labouré S, et al. ID16B: a hard X-ray nanoprobe beamline at the ESRF for nano-analysis. J Synchrotron Radiat 2016;23(1):344–52.
[44] Paganin D, Mayo SC, Gureyev TE, Miller PR, Wilkins SW. Simultaneous phase and amplitude extraction from a single defocused image of a homogeneous object. J Microsc 2002;206(1):33–40.
[45] Cloetens P, Ludwig W, Baruchel J, Van Dyck D, Van Landuyt J, Guigay J, et al. Holotomography: Quantitative phase tomography with micrometer resolution using hard synchrotron radiation x rays. Appl Phys Lett 1999;75(19):2912–4.
[46] Mirone A, Brun E, Gouillart E, Tafforeau P, Kieffer J. The PyHST2 hybrid distributed code for high speed tomographic reconstruction with iterative reconstruction and a priori knowledge capabilities. Nucl Instrum Methods Phys Res, Sect B 2014;324:41–8.
[47] Villanova J, Daudin R, Lhuissier P, Jauffres D, Lou S, Martin CL, et al. Fast in situ 3D nanoimaging: a new tool for dynamic characterization in materials science. Mater Today 2017;20(7):354–9.
[48] M.A. Paleo P, Nemoz C and Vigan'o N R, ESRF Gitlab, NABU: ESRF tomography processing software https://gitlab.esrf.fr/tomotools/nabu/.
[49] Moradi A, Sun CZ, Guan ZW, Rastegarzadeh S. Technology for lateral spreading of fibre bundles for applications in manufacturing thermoplastic composites. Compos Part a-Appl S 2023;167.
[50] Mesquita F, Swolfs Y, Lomov SV, Gorbatikh L. In-situ synchrotron computed tomography tensile testing observations of the hybrid effect: a comparison with theory. Compos Part B-Eng 2022;235.
[51] Swolfs Y, McMeeking RM, Verpoest I, Gorbatikh L. Matrix cracks around fibre breaks and their effect on stress redistribution and failure development in unidirectional composites. Compos Sci Technol 2015;108:16–22.
[52] Yang Q, Schesser D, Niess M, Wright P, Mavrogordato M, Sinclair I, et al. On crack initiation in notched, cross-plied polymer matrix composites. J Mech Phys Solids 2015;78:314–32.
[53] Zenodo 2025. https://doi.org/10.5281/zenodo.17099577.